

3D-Printed Graphene Oxide Framework with Thermal Shock Synthesized Nanoparticles for Li-CO₂ Batteries

Yun Qiao, Yang Liu, Chaoji Chen, Hua Xie, Yonggang Yao, Shuaiming He, Weiwei Ping, Boyang Liu, and Liangbing Hu*

Li-CO₂ batteries have emerged as a promising energy storage technology due to their high theoretical energy density. A thick electrode design is an effective approach for further increasing the energy density on device level by decreasing the weight and volume ratios of inactive materials. Exploring and designing novel thick electrodes with high catalytic activity toward reversible reaction between lithium and carbon dioxide are key challenges to achieve a low charge overpotential, long cycling stability, and high rate performance. Herein, an ultrathick electrode (≈ 0.4 mm) design for Li-CO₂ batteries by anchoring ultrafine Ni nanoparticles (≈ 5 nm) on a 3D-printed reduced graphene oxide framework via thermal shock (1900 K for 54 ms) is demonstrated. The cathode displays low overpotential of 1.05 V at 100 mA g⁻¹, high cycling stability of over 100 cycles, and good rate capability (up to 1000 mA g⁻¹). In particular, a high areal capacity of 14.6 mA h cm⁻² can be achieved due to the thick electrode design and uniform distribution of ultrafine catalyst nanoparticles. The strategy of combining an advanced 3D printing technique with fast thermal shock represents a promising direction toward thick electrode design in energy storage devices that are not limited to Li-CO₂ batteries.

catalysts with high activity and efficiency toward the reversible conversion between CO₂ and Li₂CO₃ is a great way to achieve the practical application of Li-CO₂ batteries.^[3] Designing metal or their compounds (metallic oxide, metallic carbide) supported on carbon materials has been proven to be an effective strategy at promoting the reversible reaction between Li and carbon dioxide.^[4] Generally, metal nanoparticles are synthesized through traditional thermal reduction techniques, using a metal salt as a precursor.^[5] However, metal nanoparticles are prone to aggregation and oxidation, which will negatively affect the catalytic active sites and electrochemical performance.^[6]

Tremendous efforts have been dedicated in the pursuit of higher energy and power densities of Li-CO₂ batteries.^[7] Among them, thick electrode design has been proven to be an effective way of achieving high energy and power density at the device level by increasing the

areal mass loading of the active materials and reducing the ratio of inactive materials.^[8] Therefore, designing a thick electrode featuring a 3D interconnected structure and controlling the particle size and distribution of the metal nanoparticles are proposed to improve the overall battery performance, yet it remains challenging to achieve these aims.^[9]

Additive manufacturing techniques, such as 3D printing, can be highly versatile and flexible in the design of complex 3D geometric shapes, composition, and function by combining computer-aided design and rapid manufacturing processes.^[10] Suitable inks that feature good shear-thinning and viscoelastic properties are vital for extrusion-based 3D printing.^[11] With well-developed inks, such as graphene oxide (GO), frameworks with various structures and shapes can be printed for diverse applications, such as consumer electronics, batteries, and solar steam generation.^[12] This technique is particularly well suited for printing thick electrodes due to its ability to scalably produce highly ordered and 3D frameworks at low manufacturing cost.^[13]


Herein, we propose an effective strategy of combining 3D printing with thermal shock treatment for the synthesis of a thick electrode design for a high energy density Li-CO₂ battery. The ultrathick (up to ≈ 0.4 mm) cathode is fabricated in two steps: first, a GO framework is constructed by 3D printing,

1. Introduction

Li-CO₂ batteries are emerging energy storage devices, which can not only contribute to reducing the greenhouse effect via CO₂ capture and the corresponding redox reaction between lithium and carbon dioxide, but are also proposed for utilization in space exploration.^[1] However, several bottlenecks have limited the application of this technology, including a high charge overpotential, low recyclability, poor rate capability, and relatively low energy density on the device level.^[2] Developing

Dr. Y. Qiao, Dr. Y. Liu
School of Chemistry and Chemical Engineering
Henan Normal University
Xinxiang, Henan 453007, P. R. China

Dr. Y. Qiao, Dr. Y. Liu, Dr. C. Chen, H. Xie, Dr. Y. Yao, S. He, W. Ping,
B. Liu, Prof. L. Hu
Department of Materials Science and Engineering
University of Maryland
College Park, MD 20742, USA
E-mail: binghu@umd.edu

 The ORCID identification number(s) for the author(s) of this article can be found under <https://doi.org/10.1002/adfm.201805899>.

DOI: 10.1002/adfm.201805899

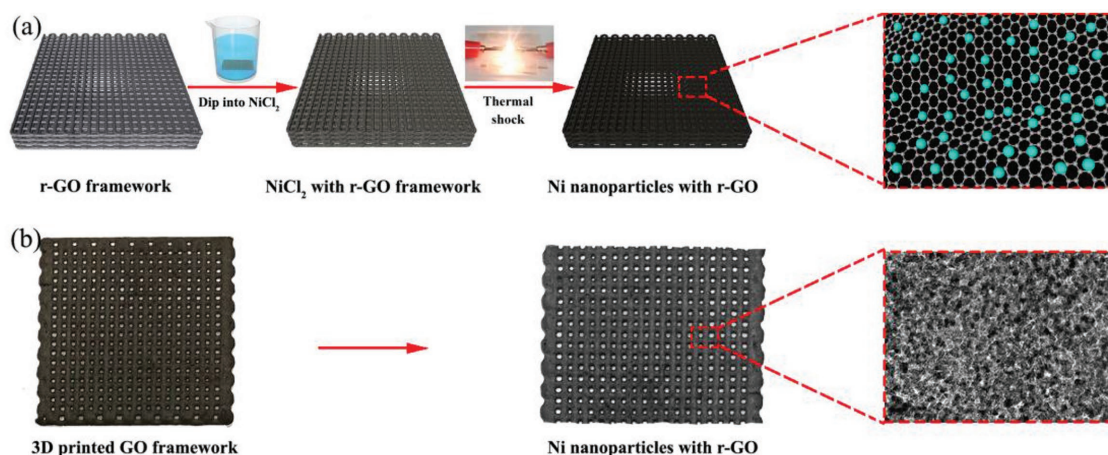


Figure 1. a) Schematic illustration of the synthesis of the 3D-printed r-GO framework, featuring thermal shock synthesized Ni nanoparticles. b) Digital images of the GO and Ni/r-GO frameworks, and the corresponding TEM image of Ni/r-GO featuring a homogeneous distribution of Ni nanoparticles anchored throughout the r-GO substrate.

followed by reduction in argon (Ar) gas at 300 °C for 1 h to obtain reduced graphene oxide (r-GO) framework; second, ultrafine Ni nanoparticles are anchored on the r-GO via fast (54 ms) and high-temperature (1900 K) thermal shock heating after dipping the framework into NiCl_2 solution. The ultrathick cathode displays a low overpotential of 1.05 V at 100 mA g^{-1} and a high areal capacity of 14.6 mA h cm^{-2} , due to the thick electrode design and uniform distribution of the ultrafine catalyst nanoparticles.

2. Results and Discussion

Figure 1a schematically illustrates the synthesis of the Ni nanoparticles anchored on the r-GO (Ni/r-GO) framework via 3D printing and thermal shock treatment. A GO multiple grid ($20 \times 20 \times 0.4$ mm) was achieved after 3D extrusion printing and freeze drying (Figure 1b and Figure S1, Supporting Information). The GO framework with 3D connected network and porous structure was then reduced to r-GO by heating under Ar atmosphere at 300 °C for 1 h, which still remains the original network and porous structure as well as the wrinkled surface (Figure S2, Supporting Information). Subsequently, the r-GO framework was dipped into NiCl_2 solution and dried in an electric oven at 80 °C for 2 h (Figure 1a). Finally, Ni nanoparticles (≈ 5 nm) can be successfully anchored on the r-GO substrate and homogeneously distributed in the whole framework via transient thermal shock (Figure 1b). The schematic illustration of the device for thermal shock is shown in Figure S3 (Supporting Information).

Figure 2a shows the temperature versus time curve of the r-GO framework with NiCl_2 during thermal shock treatment, as measured spectroscopically. The temperature gradually increased to ≈ 1900 K after 54 ms, which is enough for the decomposition of NiCl_2 into Ni nanoparticles, and then sharply cooled down in 20 ms via thermal conduction and radiation. Field-emission scanning electron microscopy (FESEM) demonstrates that the r-GO framework is maintained even after thermal shock treatment (Figure 2b–f and Figure S4,

Supporting Information). We further analyzed the distribution and fine structure of the Ni nanoparticles throughout the printed r-GO framework. The top surface shown in Figure 2c reveals the stacked r-GO filaments (the part marked in yellow) with a diameter of about 500 μm , indicating that the framework can remain in its original configuration after thermal shock. Moreover, a large number of cavities can be observed in the r-GO filaments, due to the removal of water molecules during the freeze-drying process (Figure S4, Supporting Information). This unique structure is also beneficial for the infiltration of electrolyte. As shown in Figure 2d, the corresponding high-magnification images demonstrate that a large amount of Ni nanoparticles are homogeneously distributed throughout the top portion of the framework. The Ni nanoparticles are mono-dispersed and anchored on the r-GO sheets, with an average size of ≈ 5 nm. Meanwhile, Ni nanoparticles can also be seen in middle and bottom sections of the printed r-GO framework, as shown in Figure 2e,f. These results show that the Ni nanoparticles can be uniformly anchored on the r-GO sheet in all parts of the printed framework, which is attributed to the combination of the porous structure of the framework and the fast kinetics of the thermal shock method. This highly porous network with numerous cavities is beneficial for the impregnation of NiCl_2 solution within the r-GO framework. Meanwhile, the high thermal conductivity of r-GO and ultrafast thermal shock method can enable the uniform decomposition and growth of Ni nanoparticles.

Transmission electron microscopy (TEM) images allowed us to confirm that the Ni nanoparticles are 5 ± 1 nm in diameter and highly dispersed on the printed r-GO framework (Figure 3a,b and Figure S4i,j, Supporting Information). The high-resolution TEM image of the Ni nanoparticles reveals an obvious crystal lattice with a spacing of ≈ 0.20 nm, which is assigned to the (111) plane of face-centered cubic Ni crystal (Figure 3c). The corresponding selected-area electron diffraction (SAED) pattern displays typical polycrystal diffraction rings (Figure 3d). The three diffraction rings could be indexed to (111), (200), and (220) planes of cubic nickel. Electron energy loss spectroscopy (EELS) analysis further reveals the uniform

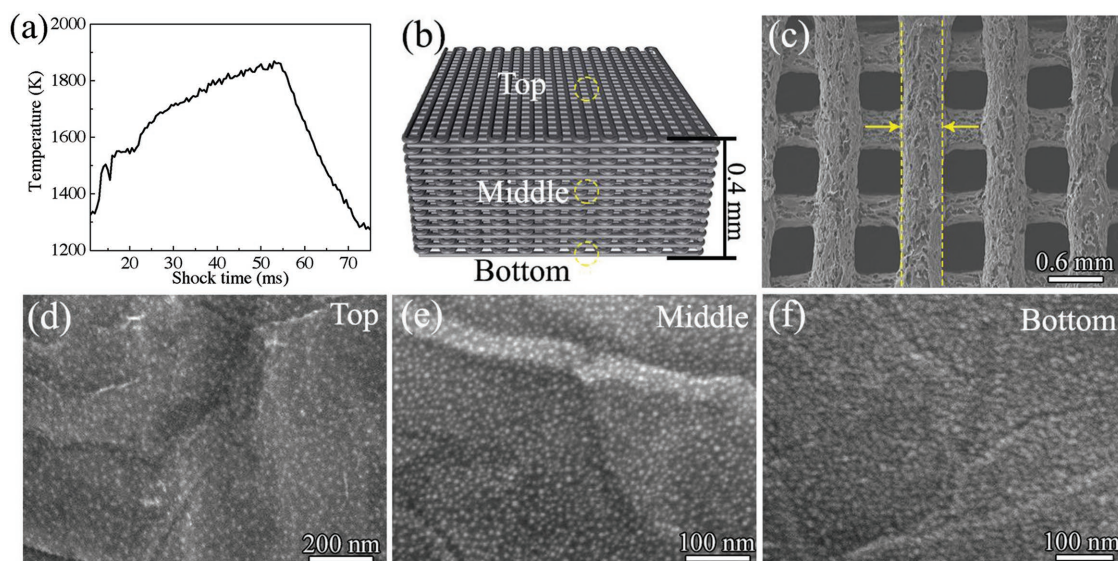


Figure 2. a) The temperature versus time curve of the r-GO framework with NiCl_2 during thermal shock treatment, as measured spectroscopically. b) Schematic illustration of the Ni/r-GO framework. c) Low-magnification FESEM images in the top section of the electrode display the interconnected grids and porous structure of the material. d–f) High-magnification FESEM images of the Ni/r-GO framework in the top section, middle cross section, and bottom section, respectively, after thermal shock treatment.

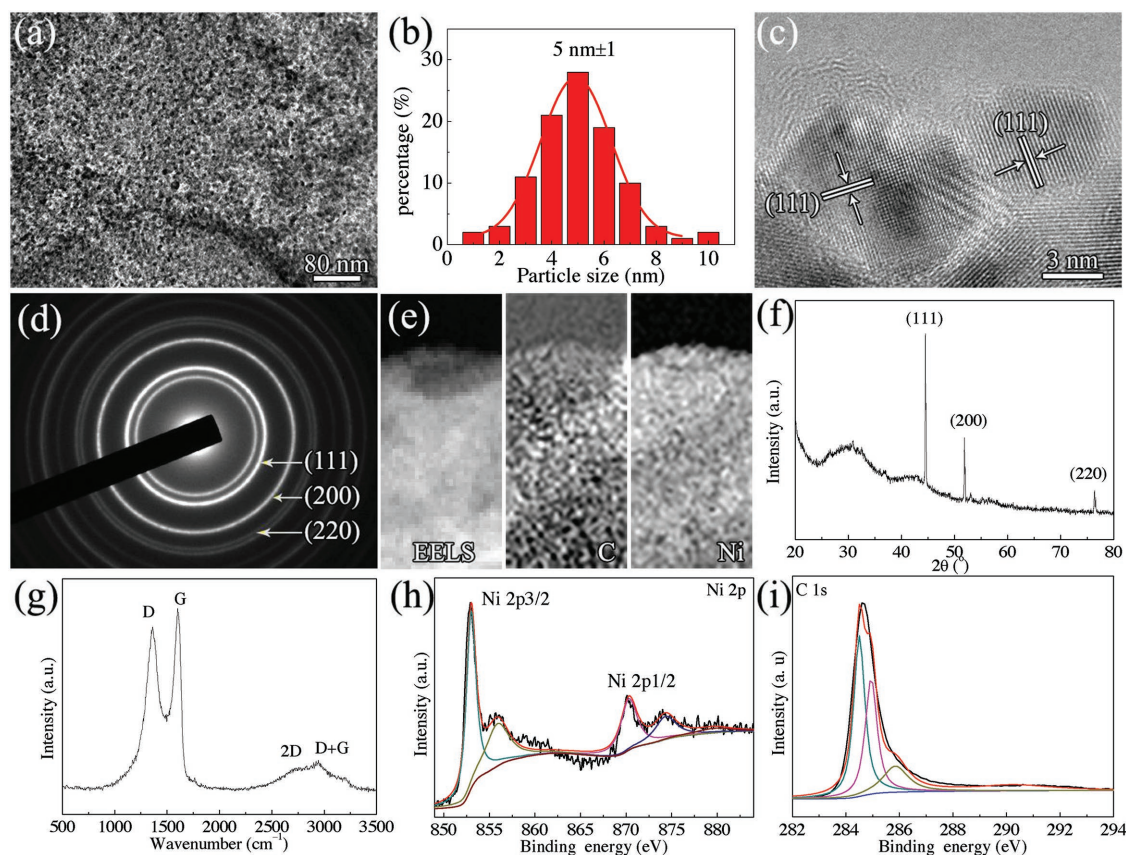


Figure 3. a) TEM image, b) particle size distribution, c) HRTEM image, d) SAED pattern, e) EELS patterns, and f) XRD pattern, as well as g) the Raman spectrum and high-resolution XPS spectra of h) Ni 2p and i) C 1s for the Ni/r-GO printed framework after the thermal shock treatment.

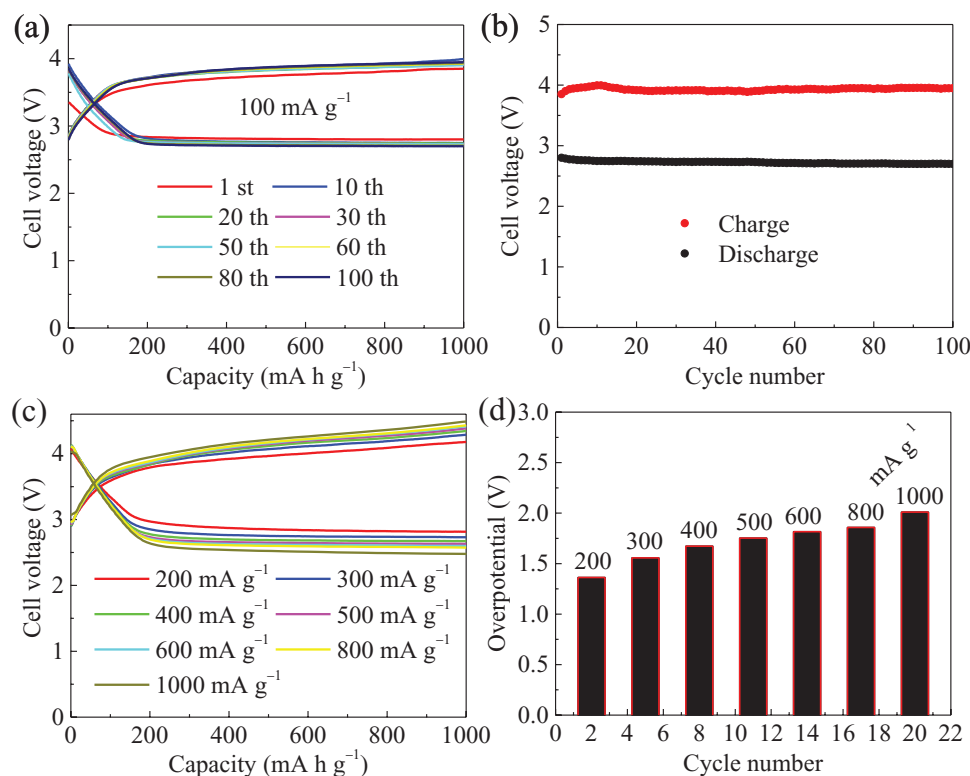


Figure 4. a) Discharge and charge curves of the Ni/r-GO framework as the cathode at a current density of 100 mA g⁻¹. b) The discharge and charge end voltages upon cycling. c) Discharge and charge curves and d) the corresponding overpotential of the cathode at various current densities with a capacity limit of 1000 mA h g⁻¹.

distribution of the Ni nanoparticles on r-GO framework (Figure 3e). The X-ray diffraction (XRD) pattern in Figure 3f demonstrates that the diffraction peaks at 2θ values of 45°, 52°, and 76° correspond to the (111), (200), and (220) planes of face-centered cubic nickel (JCPDS No. 04-0850), respectively.^[14] Furthermore, the broad peak at 31° corresponds to the typical (001) diffraction peak of graphite (JCPDS No. 74-2330). The content of Ni in r-GO framework was calculated to be 23.2 wt% via the thermogravimetric analysis (TGA), as shown in Figure S5 (Supporting Information). The Raman spectrum of the Ni/r-GO framework exhibits two peaks at 1350 cm⁻¹ (D band) and 1590 cm⁻¹ (G band), which are associated with a zone-edge A_{1g} mode (indicating the presence of disorder or imperfection), and phonon vibrations in the E_{2g} mode (sp² configuration of carbon atoms in r-GO), respectively (Figure 3g).^[15] The as-detected 2D and D+G bands can be assigned to graphitic carbon and disordered carbon in the r-GO framework, respectively.^[16]

We also performed X-ray photoelectron spectroscopy (XPS) to analyze the chemical composition of the Ni/r-GO printed framework. The high-resolution Ni 2p spectra in Figure 3h display two major peaks at 853.0 and 870.3 eV, which can be attributed to Ni 2p_{3/2} and Ni 2p_{1/2} binding energies, respectively, further confirming the nickel metal anchored on the r-GO.^[17] Moreover, the other peaks at 855.9 and 874.3 eV are related to the Ni 2p_{3/2} and Ni 2p_{1/2} of the Ni–O bond, which indicates the partial oxidation of the nickel metal. The high-resolution C 1s spectrum displays a narrow peak at 284.5 eV, which can be ascribed to nonoxygenated ring carbon in r-GO (Figure 3i).

Furthermore, the other two peaks at 285.0 and 286.0 eV can be assigned to C in C–O and C=O bonds, indicating the existence of oxygen in r-GO. In the O 1s XPS spectra, the broad peak can be deconvoluted into four peaks centered at ≈531.1, 532.0, 533.4, and 535.4 eV, which further demonstrates the existence of oxide (O²⁻), hydroxide (OH⁻), desorbed O₂, and adsorbed H₂O in the sample (Figure S6, Supporting Information).^[18]

We next examined the electrochemical properties of the Ni/r-GO as a thick cathode in a Li-CO₂ battery. **Figure 4a** presents the discharge and charge cycling performance at a current density of 100 mA g⁻¹ with a specific capacity limited to 1000 mA h g⁻¹. The electrode displays stable cycling performance and obvious potential plateaus after 100 cycles. The discharge end voltage is over 2.7 V and charge end voltage is below 4.0 V during the cycling process, which remain stable over 100 cycles (Figure 4b). Moreover, we calculated the overpotentials based on the charge and discharge end voltages, which are ≈1.05, 1.25, 1.17, 1.18, 1.17, 1.21, 1.23, and 1.25 V for the 1st, 10th, 20th, 30th, 50th, 60th, 80th to 100th cycles, respectively. These results indicate the excellent catalytic stability and durability of the Ni/r-GO framework in Li-CO₂ batteries. Figure S7 (Supporting Information) shows the initial full discharge curve of the Li-CO₂ battery at a current density of 0.1 mA cm⁻², delivering a high areal capacity of 14.6 mA h cm⁻² and the corresponding specific capacity of 8991.0 mA h g⁻¹. As shown in Figure 4c, the discharge and charge profiles of the batteries were investigated at various current densities with a capacity limit of 1000 mA h g⁻¹. All the discharge and charge voltage

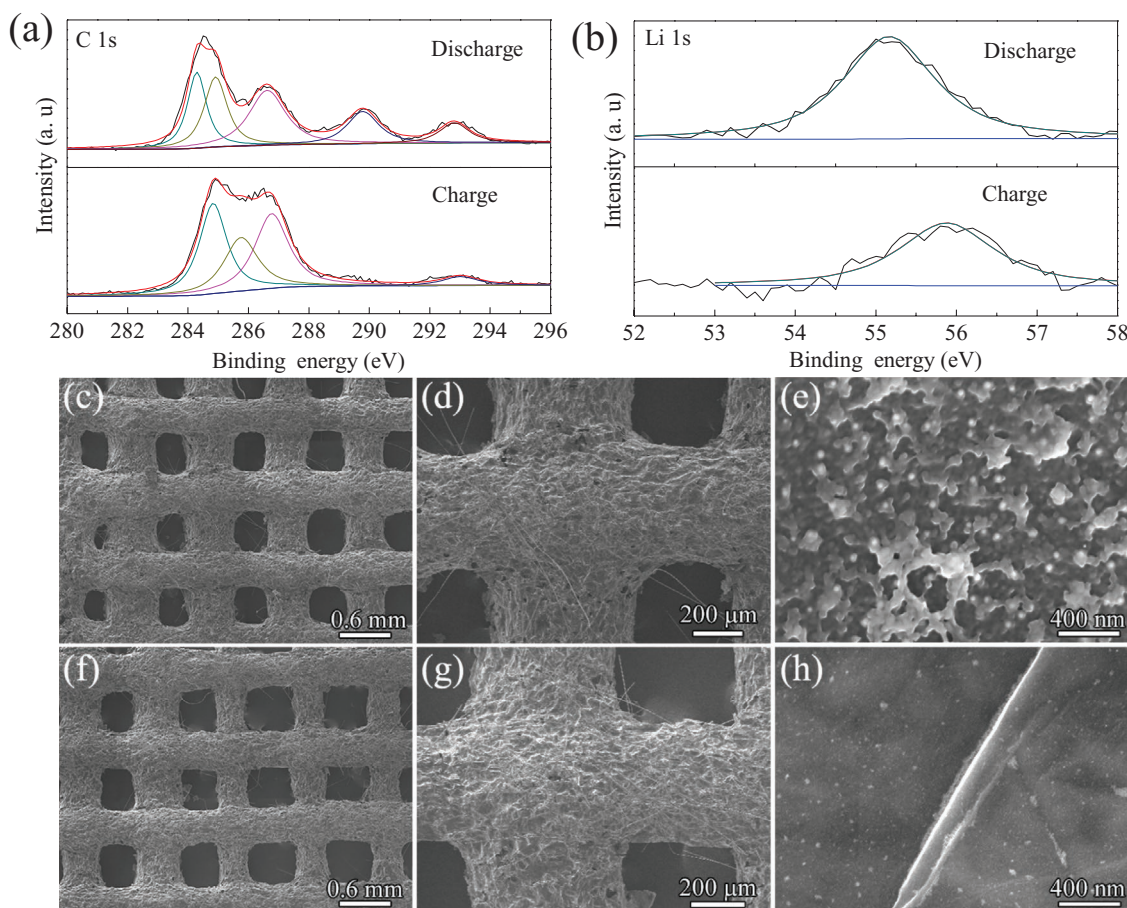


Figure 5. a) High-resolution C 1s XPS spectra after discharge and charge, demonstrating the formation of Li_2CO_3 in the discharge process and its decomposition after charge. b) High-resolution Li 1s XPS spectra after discharge and charge. FESEM images of the Ni/r-GO framework as cathode c–e) after the first discharge and f–h) after charge.

plateaus can be observed, even though the current densities increase from 200 to 1000 mA g^{-1} . The discharge end voltages are 2.81, 2.73, 2.67, 2.63, 2.60, 2.57, and 2.48 V, and the corresponding overpotentials are 1.36, 1.56, 1.67, 1.75, 1.81, 1.86, and 2.01 V at various current densities of 200, 300, 400, 500, 600, 800, and 1000 mA g^{-1} , respectively (Figure 4d). The discharge voltages are clearly improved with better rate performances than previous work on nickel-based cathode for Li-CO_2 batteries, as the as-reported maximum rate was 200 mA g^{-1} and the corresponding overpotential was 1.9 V.^[4c,d]

We further studied the chemical composition and morphology of the cathode during discharge and charge process via XPS and SEM to evaluate its reversibility. The high-resolution C 1s XPS spectra display a binding energy peak at 289.8 eV corresponding to C=O bond, indicating the deposition of Li_2CO_3 in the first discharge process, while the peak disappears after the subsequent charging process (Figure 5a).^[4c] This result indicates the formation and decomposition of Li_2CO_3 during the discharge and charge process. To verify this result, we also collected Li 1s XPS spectra, as shown in Figure 5b. The peak of Li 1s at 55.1 eV can be clearly observed, also indicating the formation of Li_2CO_3 during the first discharge process.^[19] After the subsequent charging process, the Li 1s peak at 55.1 eV disappears while a peak at 55.9 eV appears, which may be

assigned to the adsorption or decomposition of electrolyte salts on the electrode surface.^[20] Meanwhile, the ex situ XRD patterns in Figure S8 (Supporting Information) demonstrate the formation of Li_2CO_3 in the initial discharge process and its complete decomposition after the subsequent recharge process. The morphology and structure of Ni/r-GO electrode were further characterized after the initial discharge and charge. The low-magnification FESEM images confirm that the framework structure remains intact after discharging (Figure 5c,d) and even charging (Figure 5f,g). However, the high-magnification FESEM images demonstrate that a large number of irregular structures and some spherical particles (Li_2CO_3) are deposited on the electrode surface after the full discharge process (Figure 5e). Moreover, these irregular and sphere-like particles disappear after the full charge process, indicating the discharge product of Li_2CO_3 can be decomposed, which agrees well with the XPS analysis (Figure 5h). These results demonstrate that the catalytic activity of the Ni/r-GO framework toward the decomposition of Li_2CO_3 is excellent.

The Ni/r-GO framework exhibits several unique properties with high-temperature treatment at ≈ 1900 K, positioning it as a promising Li- CO_2 cathode material. First, the 3D printing frame structure with open channels can offer highly efficient diffusion pathways for carbon dioxide. Moreover, the highly

porous network within the filament structure can also promote permeation of the electrolyte. Second, the highly interconnected Ni/r-GO framework can provide a conductive network to ensure excellent electron transport properties. Third, the Ni/r-GO framework with uniform distribution of ultrafine Ni nanoparticles could promote the catalytic activity and improve the reversibility between lithium and carbon dioxide. Finally, the 3D-printed thick electrode is an effective way to achieve high energy and power density at device level and thus can further promote the practical application of Li-CO₂ batteries.

3. Conclusion

For the first time, 3D printing technology was combined with thermal shock synthesis to produce an ultrathick (up to ≈0.4 mm) cathode composed of a Ni/r-GO framework for Li-CO₂ batteries. The electrode framework was fabricated using GO inks via extrusion-based 3D printing, followed by reduction to r-GO. After the in situ thermal decomposition of metal salts via thermal shock at ≈1900 K for 54 ms, ≈5 nm Ni nanoparticles can be anchored to the r-GO framework. As the cathode in a Li-CO₂ battery, the Ni/r-GO framework can deliver a high areal capacity of 14.6 mA h cm⁻² in the initial discharge process. Moreover, the battery presents a stable cycling performance for 100 cycles, a high rate performance of up to 1000 mA g⁻¹, and a discharge and charge overpotential as low as 1.05 V. This work offers an effective and convenient strategy to design thick electrodes with high catalytic activity for high-performance energy storage devices, which are not limited to Li-CO₂ batteries.

4. Experimental Section

Preparation of the GO Framework: GO was prepared by graphite powder using a modified Hummer's method.^[21] 200 mg GO was dispersed in 0.5 mL deionized (DI) water using a mortar to grind the material into a smooth paste. The as-prepared ink was then transferred into a 10 mL syringe for further use. The procedure was set up to print the GO framework using a panel pad connecting with 3D printer machine (F4200N Compact Benchtop Robot, Fisanar). The printing line size could be controlled by setting the printing rate on the panel pad and using a Fisanar DSP501N air-powered fluid dispenser. After printing, the GO framework was freeze dried at -50 °C to dehydrate and dry the material (FreeZone 2.5, Labconco).

Preparation of Ni/r-GO: The dried GO framework was thermally reduced at 300 °C for 1 h under Ar atmosphere to obtain the r-GO framework, which was then dipped into 0.05 mol L⁻¹ NiCl₂ (Sigma-Aldrich) aqueous solution with vacuum treatment to absorb NiCl₂ solution into the r-GO cavities. Then, the NiCl₂ with r-GO framework was dried at 80 °C in an electric oven for 2 h. The framework was connected to two copper electrodes and fixed on glass slides with silver paste, then transferred into an Ar-filled glovebox for thermal shock treatment to obtain the final Ni/r-GO electrode material. A spectrometer (Ocean Optics, Inc.) coupled with an optical fiber was used to collect the emitted light. The measurement system was calibrated by a National Institute of Standards and Technology (NIST) traceable light source. The temperature is calculated by fitting the emitted light spectra basing on the gray body radiation and the following equation^[22]

$$B_{\lambda}(\lambda, T) = \gamma \epsilon_{\text{gray}} \frac{2hc^2}{\lambda^5} \frac{1}{e^{hc/\lambda k_B T} - 1} \quad (1)$$

where k_B is the Boltzmann constant, λ is the wavelength, h is the Planck's constant, c is the speed of light, and ϵ_{gray} is the gray body emissivity, the scaling constant γ and temperature T are fitting parameters for this equation.

Material and Electrochemical Characterization: The morphology of the samples was observed using a SU-70 FESEM. TEM images and EELS spectra were collected on a JEM 2100 FEG electron microscope. XRD patterns were performed to check the phase of the samples using an D8 Advanced Diffractometer (Bruker AXS, WI, USA). The TGA measurements were performed on Discovery SDT650 (TA Instruments) with a heating rate of 10 °C min⁻¹ under air atmosphere. XPS spectra were obtained on a Kratos Axis 165 X-ray photoelectron spectrometer.

Coin cells (CR 2032-type) were assembled using the Ni/r-GO framework as the cathode, glass fiber as the separator, lithium metal as the anode, and 1.0 mol L⁻¹ bis(trifluoromethane) sulfonimide lithium salt (LiTFSI) in tetraethylene glycol dimethyl etherdimethyl sulfoxide (TEGME) as the electrolyte. Cyclic voltammetry (CV) curves were carried out on Gamry Reference 3000 Potentiostat/Galvanostat/ZRA. The galvanostatic charge and discharge cycling performances were measured on a CT2001A LAND system.

Supporting Information

Supporting Information is available from the Wiley Online Library or from the author.

Acknowledgements

Y.Q. and Y.L. contributed equally to this work. The authors acknowledge the support of the Maryland NanoCenter, its Surface Analysis Center and AIMLab. The authors acknowledge Michael R. Zachariah lab for the temperature profile measurement (with Y.Y.'s help). Y.Q. and Y.L. acknowledge the financial support of the National Natural Science Foundation of China (Grant Nos. 21501049 and 21503071) and the China Scholarship Council (CSC, Grant Nos. 201608410042 and 201508410200).

Conflict of Interest

The authors declare no conflict of interest.

Keywords

3D printing, graphene oxide, Li-CO₂ battery, nickel nanoparticles, thermal shock

Received: August 23, 2018

Revised: October 8, 2018

Published online:

- [1] a) Z. Xie, X. Zhang, Z. Zhang, Z. Zhou, *Adv. Mater.* **2017**, 29, 1605891; b) C. Li, Z. Guo, B. Yang, Y. Liu, Y. Wang, Y. Xia, *Angew. Chem., Int. Ed.* **2017**, 56, 9126; c) A. Douglas, N. Muralidharan, R. Carter, C. L. Pint, *ACS Sustainable Chem. Eng.* **2017**, 5, 7104.
- [2] X. Hu, Z. Li, J. Chen, *Angew. Chem., Int. Ed.* **2017**, 56, 5785.
- [3] a) Z. Zhang, Q. Zhang, Y. Chen, J. Bao, X. Zhou, Z. Xie, J. Wei, Z. Zhou, *Angew. Chem., Int. Ed.* **2015**, 54, 6550; b) S. Xu, S. K. Das, L. A. Archer, *RSC Adv.* **2013**, 3, 6656; c) Y. Qiao, J. Yi, S. Wu, Y. Liu, S. Yang, P. He, H. Zhou, *Joule* **2017**, 1, 359; d) Y. Liu, R. Wang, Y. Lyu, H. Li, L. Chen, *Energy Environ. Sci.* **2014**, 7, 677.

- [4] a) Z. Zhang, Z. Zhang, P. Liu, Y. Xie, K. Cao, Z. Zhou, *J. Mater. Chem. A* **2018**, 6, 3218; b) Y. Hou, J. Wang, L. Liu, Y. Liu, S. Chou, D. Shi, H. Liu, Y. Wu, W. Zhang, J. Chen, *Adv. Funct. Mater.* **2017**, 27, 1700564; c) X. Zhang, C. Wang, H. Li, X. G. Wang, Y. N. Chen, Z. Xie, Z. Zhou, *J. Mater. Chem. A* **2018**, 6, 2792; d) Z. Zhang, X. G. Wang, X. Zhang, Z. Xie, Y. N. Chen, L. Ma, Z. Peng, Z. Zhou, *Adv. Sci.* **2018**, 5, 1700567; e) L. Qie, Y. Lin, J. W. Connell, J. Xu, L. Dai, *Angew. Chem., Int. Ed.* **2017**, 56, 6970.
- [5] S. Yang, Y. Qiao, P. He, Y. Liu, Z. Cheng, J. Zhu, H. Zhou, *Energy Environ. Sci.* **2017**, 10, 972.
- [6] a) X. Wang, J. Feng, Y. Bai, Q. Zhang, Y. Yin, *Chem. Rev.* **2016**, 116, 10983; b) C. Zhu, D. Du, A. Eychmüller, Y. Lin, *Chem. Rev.* **2015**, 115, 8896; c) F. Zou, Y. M. Chen, K. Liu, Z. Yu, W. Liang, S. M. Bhaway, M. Gao, Y. Zhu, *ACS Nano* **2016**, 10, 377; d) A. Douglas, R. Carter, M. Li, C. L. Pint, *ACS Appl. Mater. Interfaces* **2018**, 10, 19010.
- [7] a) C. Chen, Y. Zhang, Y. Li, Y. Kuang, J. Song, W. Luo, Y. Wang, Y. Yao, G. Pastel, J. Xie, L. Hu, *Adv. Energy Mater.* **2017**, 7, 1700595; b) Y. Liu, B. Zhang, Q. Xu, Y. Hou, S. Seyedin, S. Qin, G. G. Wallace, S. Beirne, J. M. Razal, J. Chen, *Adv. Funct. Mater.* **2018**, 28, 1706592; c) X. Tian, J. Jin, S. Yuan, C. K. Chua, S. B. Tor, K. Zhou, *Adv. Energy Mater.* **2017**, 7, 1700127.
- [8] a) T. S. Wei, B. Y. Ahn, J. Grotto, J. A. Lewis, *Adv. Mater.* **2018**, 30, 1703027; b) Z. Du, K. M. Rollag, J. Li, S. J. An, M. Wood, Y. Sheng, P. P. Mukherjee, C. Daniel, D. L. Wood, *J. Power Sources* **2017**, 354, 200; c) C. Chen, Y. Zhang, Y. Li, J. Dai, J. Song, Y. Yao, Y. Gong, I. Kierzewski, J. Xie, L. Hu, *Energy Environ. Sci.* **2017**, 10, 538.
- [9] a) Z. Tu, M. J. Zachman, S. Choudhury, S. Wei, L. Ma, Y. Yang, L. F. Kourkoutis, L. A. Archer, *Adv. Energy Mater.* **2017**, 7, 1602367; b) Z. Wang, K. Fu, Z. Liu, Y. Yao, J. Dai, Y. Wang, B. Liu, L. Hu, *Adv. Funct. Mater.* **2017**, 27, 1605724; c) H. M. Cheng, F. Li, *Science* **2017**, 356, 582.
- [10] a) K. Fu, Y. Yao, J. Dai, L. Hu, *Adv. Mater.* **2017**, 29, 1603486; b) Y. Liu, Y. Qiao, Y. Zhang, Z. Yang, T. Gao, D. Kirsch, B. Liu, J. Song, B. Yang, L. Hu, *Energy Storage Mater.* **2018**, 12, 197; c) M. K. Hausmann, P. A. Rühs, G. Siqueira, J. Läger, R. Libanori, T. Zimmermann, A. R. Studart, *ACS Nano* **2018**, 12, 6926.
- [11] a) A. Ambrosi, J. G. S. Moo, M. Pumera, *Adv. Funct. Mater.* **2016**, 26, 698; b) G. Siqueira, D. Kokkinis, R. Libanori, M. K. Hausmann, A. S. Gladman, A. Neels, P. Tingaut, T. Zimmermann, J. A. Lewis, A. R. Studart, *Adv. Funct. Mater.* **2017**, 27, 1604619; c) K. Yang, J. C. Grant, P. Lamey, A. Joshi-Imre, B. R. Lund, R. A. Smaldone, W. Voit, *Adv. Funct. Mater.* **2017**, 27, 1700318.
- [12] a) R. D. Sochol, E. Sweet, C. C. Glick, S. Y. Wu, C. Yang, M. Restaino, L. Lin, *Microelectron. Eng.* **2018**, 189, 52; b) Y. Li, T. Gao, Z. Yang, C. Chen, W. Luo, J. Song, E. Hitz, C. Jia, Y. Zhou, B. Liu, B. Yang, L. Hu, *Adv. Mater.* **2017**, 29, 1700981; c) K. Share, A. P. Cohn, R. Carter, B. Rogers, C. L. Pint, *ACS Nano* **2016**, 10, 9738; d) K. Liu, Y. M. Chen, G. M. Policastro, M. L. Becker, Y. Zhu, *ACS Nano* **2015**, 9, 6041.
- [13] F. Zhang, M. Wei, V. V. Viswanathan, B. Swart, Y. Shao, G. Wu, C. Zhou, *Nano Energy* **2017**, 40, 418.
- [14] W. Ni, B. Wang, J. Cheng, X. Li, Q. Guan, G. Gu, L. Huang, *Nanoscale* **2014**, 6, 2618.
- [15] Y. Liu, Y. Qiao, G. Wei, S. Li, Z. Lu, X. Wang, X. Lou, *Energy Storage Mater.* **2018**, 11, 274.
- [16] Y. Li, Y. Chen, A. Nie, A. Lu, R. J. Jacob, T. Gao, J. Song, J. Dai, J. Wan, G. Pastel, M. R. Zachariah, R. S. Yassar, L. Hu, *Adv. Energy Mater.* **2017**, 7, 1601783.
- [17] M. A. Peck, M. A. Langell, *Chem. Mater.* **2012**, 24, 4483.
- [18] a) J. Ding, H. Wang, Z. Li, K. Cui, D. Karpuzov, X. Tan, A. Kohandehghan, D. Mitlin, *Energy Environ. Sci.* **2015**, 8, 941; b) Y. Liu, Z. Q. Gao, *Energy Technol.* **2017**, 5, 481.
- [19] S. Choudhury, C. T.-C. Wan, W. I. Al Sadat, Z. Tu, S. Lau, M. J. Zachman, L. F. Kourkoutis, L. A. Archer, *Sci. Adv.* **2017**, 3, e1602809.
- [20] S. Contarini, J. W. Rabalais, *J. Electron Spectrosc. Relat. Phenom.* **1985**, 35, 191.
- [21] W. S. Hummers, R. E. Offeman, *J. Am. Chem. Soc.* **1958**, 80, 1339.
- [22] Y. Zhou, B. Natarajan, Y. Fan, H. Xie, C. Yang, S. Xu, Y. Yao, F. Jiang, Q. Zhang, J. W. Gilman, L. Hu, *Angew. Chem., Int. Ed.* **2018**, 57, 2625.